

Article

Effect of Control Measures on Wheel/Rail Noise When the Vehicle Curves

Jian Han ¹, Yuanpeng He ¹, Xinbiao Xiao ^{1,*}, Xiaozhen Sheng ^{1,*}, Guotang Zhao ^{1,2} and Xuesong Jin ¹

¹ State Key Laboratory of Traction Power, Southwest Jiaotong University, Chengdu 610031, China; hanjianswjtu@gmail.com (J.H.); yuanpenghe@gmail.com (Y.H.); guotangzhao@gmail.com (G.Z.); xsjin@swjtu.edu.cn (X.J.)

² China Railway Corporation, Beijing 100844, China

* Correspondence: xiao@home.swjtu.edu.cn (X.X.); shengxiaozhen@swjtu.edu.cn (X.S.); Tel.: +86-135-4079-1500 (X.X.); +86-180-3069-0757 (X.S.)

Received: 12 October 2017; Accepted: 3 November 2017; Published: 6 November 2017

Abstract: This paper developed a time domain simplified model to study the effect of control measures on wheel/rail noise when the vehicle curves. The time domain model consists of two parts, one being a vehicle-track coupling dynamic model for wheel/rail interaction, the other being a transient finite element and boundary element domain model for vibration and sound radiation. Wheel/rail noise under wheel/rail lateral creep force is predicted for a narrowly curved section of a conventional underground railway, and compared with measurement. Based on the developed model, the effect of wheel/rail friction modification on squeal noise is investigated. In addition, effectiveness of resilient wheel and embedded track to control curve squeal noise are also assessed.

Keywords: wheel/rail noise; vehicle/track dynamic model; wheel/rail friction modification; resilient wheel; embedded track

1. Introduction

Railway squeal noise is difficult to study because of its mechanism, wheel/rail interaction and random acoustic behaviour. Squeal generates as a railway vehicle negotiates a narrow curve, producing a tonal noise of high amplitude. Typically, the noise is radiated from the wheels and has most of its energy between 400 Hz and 10 kHz (in the frequency band where human beings are most sensitive to noise). In the process of curving, a series of railway wheel modes (particularly the wheel's axial modes) are easy to be excited, which may lead to curve squeal [1–3]. Known practical solutions for railway squeal in a particular curve include friction modification [4,5] and wheel damping treatments [6–9]. These solutions can reduce the occurrence of squeal for some special circumstance.

Curve squeal noise has received increased attention by means of simulations and tests. Most previous research considered that the mechanism of railway curve squeal is mainly a kind of self-excited vibration due to the nonlinear creep forces [1,3,10–19]. Rudd [1] found that the main excitation mechanisms of squeal were related to lateral direction stick-slip phenomena which introduced unstable wheel/rail forces and vibrations. Slope of the creep force-creepage curve becomes negative instead of a constant value when the creepages reach a high level. Many models to simulate curve squeal were developed based on Rudd's squeal theory. Most of the models begin with a characteristic of the creepage-dependent friction coefficient. Van Ruiten [10], for example, applied Rudd's model to trams. In a review article, Remington [11] described the state of the art of railway curve squeal up to 1985. He suggested that this model should include finite element models of railway wheel dynamics, numerical models for the dynamics of bogies in curves and details of the friction coefficient versus creepage. Since then, Schneider et al. [12] developed a modal model for the wheel and calculated its

self-excited vibrations in the time domain through introducing Kraft's formula for the falling friction coefficient in the sliding region. Fingberg [13] included a finite element model of the wheelset and a modal model of the rail. The creep force formula is derived from Kalker's theory [20] of rolling contact, extended to include a falling regime based on Kraft's formula to resemble experimental findings more closely at large creepages. Fingberg's work has been extended further by Périard [14] who included vehicle dynamics simulations in a time-domain curve squeal calculation. Xie [21] introduced a simplified friction law into SIMPACK using a modified FASTSIM for curve squeal calculations based on Fingberg's work and TWINS. Heckl [16] developed an annular disc model and analyzed its vibration response in time domain. Heckl's work made a contribution to understanding of the disc vibration and its modal shapes when squeal noise occurs due to lateral creepage. In order to consider railway wheel geometry, Heckl's model needs to be improved. De Beer et al. [16] also presented a curve squeal model considering lateral creepages. The difference was that his model was developed in frequency domain. Noise radiation was predicted using the standard components of the TWINS software [22]. The model of de Beer was extended by Monk-Steel and Thompson [17] by including the case of wheel flange contact, which usually occurred at the leading wheel at high rail. Chiello et al. [18] presented a curve squeal model including not only tangential dynamics (friction force) but also normal dynamics on the wheel/rail contact zone. The model can predict the unstable wheel modes and the corresponding squeal level and spectrum. Huang [23] reviewed the curve squeal models, and developed a curve squeal model including a self-excited loop and relationship between wheel/rail motions and contact forces. A number of authors have proposed an alternative mechanism based on 'mode coupling', which has been explained in a simplified form by Hoffmann et al. [24,25], see also [26]. More recently Thompson comprehensively reviewed two mechanisms ('falling friction' and 'mode coupling'), experimental and theoretical work in the field of curve squeal and discussed mitigation measures in terms of these two mechanisms [27].

This paper developed a time domain simplified model to study the effect of control measures on wheel/rail noise when the vehicle curves. This model, different from the self-excited vibration model, mainly analyzed the wheel/rail noise characteristic under lateral excitation. Wheel/track vibration and sound pressure can approximate predicted for a vehicle negotiating a narrow curve. The effects of lubricant between wheel/rail interface, elastic wheel, and embedded track on wheel/rail noise reduction under lateral excitation are investigated.

2. The Time Domain Model for Predicting Wheel/Rail Noise under Lateral Excitation

2.1. Vehicle/Track Interaction Model with Falling Friction Coefficients

Figure 1 shows a three-dimensional dynamic model of a metro vehicle which coupled with a conventional ballastless track which can predict the curve squeal when a vehicle negotiates narrow curves. The dynamic model is based on the classical dynamic theory, which was also successfully applied to many research topics in rail transit field [28–33]. In this paper, the car-body and two bogies are modelled as rigid bodies. The primary and secondary suspensions are modelled as spring-damp elements. The track system is a triple-layers model as demonstrated in [30], in which the couple of rails are modelled as Timoshenko beams. The explicit integration method in [34] is used to solve dynamic equations.

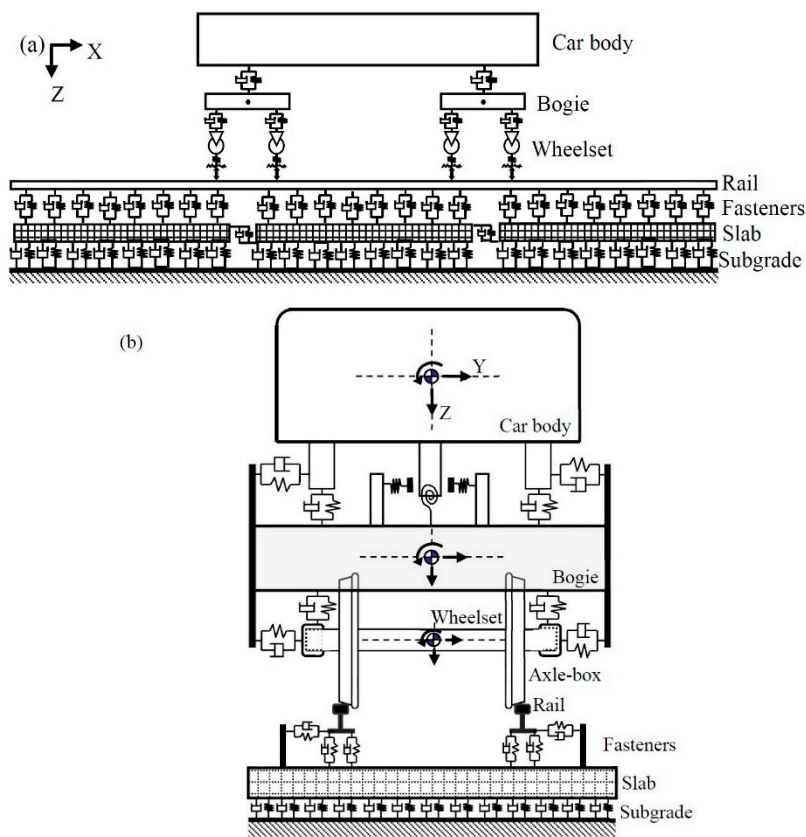


Figure 1. Coupling dynamic model of a metro vehicle and a conventional ballastless track: (a) Elevation; (b) End view.

Wheel-rail normal force is calculated based on non-linear Hertzian contact theory. Non-linear Hertzian contact force is simulated by Equation (1). The normal force depends on the relationship between normal loading and wheel, rail deformation if the normal compression at the wheel/rail contact point is larger than zero when wheel and rail are in contact. The normal force is zero if the normal compression at the wheel/rail contact point is not larger than zero when the wheel and rail separates.

$$N(t) = \begin{cases} [\frac{1}{G_{Hertz}} Z_{wrnc}(t)]^{3/2}, & Z_{wrnc}(t) > 0 \\ 0, & Z_{wrnc}(t) \leq 0 \end{cases} \quad (1)$$

where G_{Hertz} is the contact constant of wheel and rail ($m/N^{2/3}$). For LM wheel tread profile and CN60 rail, $G_{Hertz} = 3.86 R^{-0.115} \times 10^{-8}$. R is the wheel rolling radius. $Z_{wrnc}(t)$ is the normal compression at the wheel/rail contact point.

The tangential creep forces of wheel and rail are calculated based on Kalker's simplified creep theory, in which the falling down friction law [13] is introduced. The contact area is discretized and the tangential wheel-rail creep force is solved through iteration from the leading part of the contact area to its trailing part. Thus, the tangential wheel-rail creep forces can be written as follows:

$$\begin{cases} p_{xi} = p_{x(i-1)} - \left(\frac{\xi_x}{L_1} - \frac{\xi_z y_i}{L_3} \right) \Delta x \\ p_{yi} = p_{y(i-1)} - \left(\frac{\xi_y}{L_2} - \frac{\xi_z (x_i + 0.5 \Delta x)}{L_3} \right) \Delta x \end{cases} \quad (2)$$

where p_{xi} and p_{yi} are longitudinal and lateral tangential wheel-rail creep force. ξ_x, ξ_y, ξ_z are longitudinal, lateral and spin creepage, respectively. Δx is the longitudinal width of discrete grid. L_1, L_2, L_3 are flexibility coefficients and can be written as follows:

$$L_1 = \frac{8a}{3GC_{11}}, L_2 = \frac{8a}{3GC_{22}}, L_3 = \frac{\pi a \sqrt{a/b}}{4GC_{23}} \tag{3}$$

where a and b are the lengths of longitudinal and lateral semi-axis, respectively. G is the shear modulus of wheel/rail. C_{ij} is the coefficient calculated by Kalker in 1967 [20].

The tangential wheel-rail creep forces at any point of contact area can be written as follows:

$$p_{ti} = \sqrt{p_{xi} + p_{yi}} \tag{4}$$

If

$$p_{ti} \leq \mu p_n(x, y) \tag{5}$$

where μ is the wheel/rail friction coefficient, and p is the distribution of wheel/rail normal force, the particle in contact area is in an adhesion state. The tangential wheel-rail creep forces can be calculated by Equation (2).

If

$$p_{ti} > \mu p_n(x, y) \tag{6}$$

the particle in contact area is in a slide state. The tangential wheel-rail creep forces can be reduced to Equation (7):

$$\begin{cases} p_{xi} = p_{xi} \left(\frac{\mu p_n(x,y)}{p_{ti}} \right) \\ p_{yi} = p_{yi} \left(\frac{\mu p_n(x,y)}{p_{ti}} \right) \end{cases} \tag{7}$$

The wheel/rail friction coefficient μ can be modeled by a constant [35], Fingberg law (Equation (8)) [13] or piecewise friction coefficient (Equation (9)) [21].

$$\mu(x, y) = \mu_s \left[\frac{50}{100 + |\mathbf{v}(x, y)|^2} + \frac{0.1}{0.2 + |\mathbf{v}(x, y)|} \right] \tag{8}$$

where $\mathbf{v}(x, y)$ is the slip velocity between rail and wheel, μ_s is the static friction coefficient.

$$\mu(x, y) = \begin{cases} \mu_s & \text{if } |\mathbf{v}(x, y)| = 0 \\ \mu_s - \frac{\mu_s - \mu_d}{v_c} \cdot |\mathbf{v}(x, y)| & \text{if } 0 < |\mathbf{v}(x, y)| \leq v_c \\ \mu_d & \text{if } |\mathbf{v}(x, y)| > v_c \end{cases} \tag{9}$$

where μ_d is the sliding friction coefficient, v_c the critical sliding velocity, and $\mathbf{v}(x, y)$ is the slip velocity in the local coordinate system.

Figure 2 gives the relationship of Creep force and Creepage based on three kinds of friction coefficients. The Fingberg model and piecewise model both consider the falling down friction coefficient. The piecewise friction coefficient is simplified from Fingberg model. The falling friction coefficient needs to be taken into account in the process of curve squeal simulation. This study used the Fingberg’ model.

In this study, a special type of track, i.e., embedded track, is investigated. Figure 3 shows the dynamic model of filling material (including elastomer and rail pad) in the groove. The filling material is glued to the rail and slab, and it provides elastic support and damping. There is no relative motion between filling material and rail/slab. In the dynamic simulation of embedded track, the filling material of the embedded track is approximately simulated as mass-spring-damping system. Compared with the spring-damping simulation, the effects of the inertia of elastomer can be considered

in the mass-spring-damping system in this paper. The slab of the embedded track is simulated by 3D finite element in the vehicle-track coupling dynamic model.

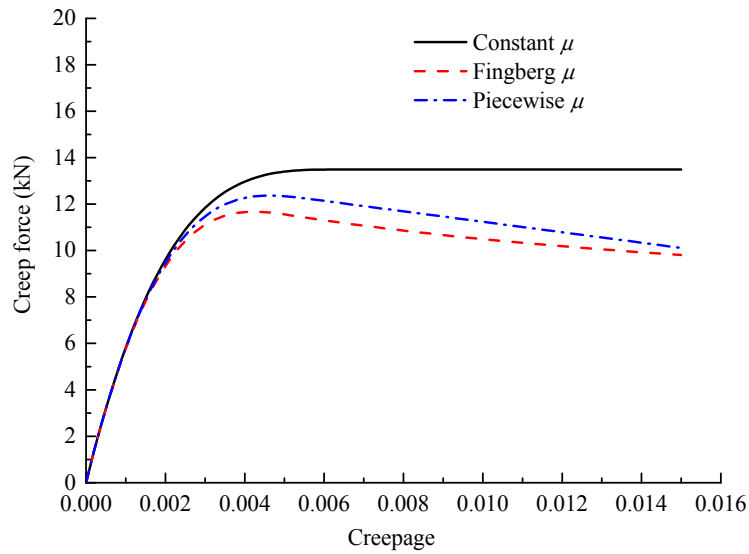


Figure 2. Creep force-Creepage relationship based on three kinds of friction coefficients.

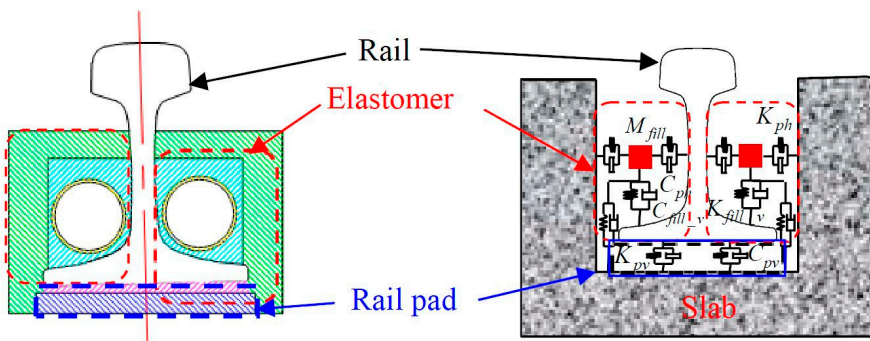


Figure 3. Dynamic model of filling material in groove.

Figure 4 shows the force diagram of elastomer of filling material (the mass in Figure 3). The lateral and vertical motions of elastomer of filling material on left side and right side of the one rail are written in Equations (10)–(13). The stiffness (K_{ph} and K_{fill_v}) and damping (C_{ph} and C_{fill_v}) are including in forces in Figure 4.

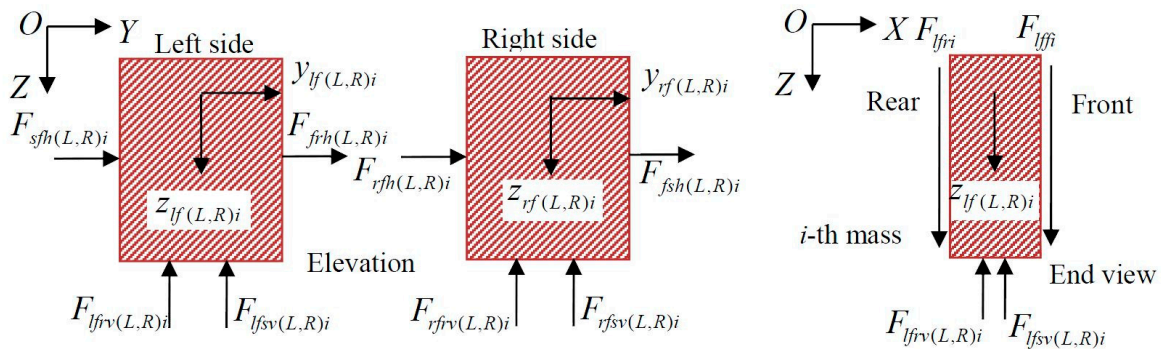


Figure 4. Dynamic model of elastomer in groove.

Lateral motion equation of elastomer on the left side

$$M_{filli}\ddot{y}_{lf(L,R)i} = F_{sfh(L,R)i} + F_{frh(L,R)i} \tag{10}$$

Vertical motion equation of elastomer on the left side

$$M_{filli}\ddot{z}_{lf(L,R)i} = -F_{lfrv(L,R)i} - F_{lfsv(L,R)i} + F_{lff(L,R)i} + F_{lfr(L,R)i} \tag{11}$$

Lateral motion equation of elastomer on the right side

$$M_{filli}\ddot{y}_{rf(L,R)i} = F_{fsh(L,R)i} + F_{rfh(L,R)i} \tag{12}$$

Vertical motion equation of elastomer on the right side

$$M_{filli}\ddot{z}_{rf(L,R)i} = -F_{rfrv(L,R)i} - F_{rfsv(L,R)i} + F_{rff(L,R)i} + F_{rfr(L,R)i} \tag{13}$$

where M_{filli} is the mass of the i -th elastomer on one side (left or right) of the rail. $\ddot{z}_{lf(L,R)i}$ and $\ddot{z}_{rf(L,R)i}$ are vertical accelerations of the i -th elastomer on the left and right sides of the rail. $\ddot{y}_{lf(L,R)i}$ and $\ddot{y}_{rf(L,R)i}$ are lateral accelerations of the i -th elastomer on the left and right sides of the rail. $F_{sfh(L,R)i}$ ($F_{fsh(L,R)i}$) and $F_{frh(L,R)i}$ ($F_{rfh(L,R)i}$) are lateral force between slab and elastomer, and lateral force between elastomer and rail. $F_{lfrv(L,R)i}$, $F_{lfsv(L,R)i}$, $F_{lff(L,R)i}$ and $F_{lfr(L,R)i}$ are vertical force between elastomer and rail, vertical force between elastomer and slab, vertical force between the i -th and the $(i - 1)$ -th elastomers, and vertical force between the i -th and the $(i + 1)$ -th elastomers on the left side. $F_{rfrv(L,R)i}$, $F_{rfsv(L,R)i}$, $F_{rff(L,R)i}$ and $F_{rfr(L,R)i}$ are vertical force between elastomer and rail, vertical force between elastomer and slab, vertical force between the i -th and the $(i - 1)$ -th elastomers, and vertical force between the i -th and the $(i + 1)$ -th elastomers on the right side.

In addition to the embedded track, the resilient wheel is also examined. Figure 5 shows the dynamic model of resilient wheel. The lateral and vertical motions of resilient wheel are written in Equations (14)–(19).

$$M_{w1}[\ddot{Y}_{1wL,Ri} + \frac{V^2}{R_{wi}} + R\ddot{\phi}_{sewi}] = -F_{eyL,Ri} + F_{wryL,Ri} + M_{w1}g\phi_{sewi} \tag{14}$$

$$M_{w1}[\ddot{Z}_{1wL,Ri} - a_0\ddot{\phi}_{sewi} - \frac{V^2}{R_{wi}}\phi_{sewi}] = F_{ezL,Ri} - F_{w rzL,Ri} + M_{w1}g \tag{15}$$

$$M_{w2}[\ddot{Y}_{2wi} + \frac{V^2}{R_{wi}} + R\ddot{\phi}_{sewi}] = -F_{fyLi} - F_{fyRi} + F_{eyLi} + F_{eyRi} + M_{w2}g\phi_{sewi} \tag{16}$$

$$M_{w2}[\ddot{Z}_{2wi} - a_0\ddot{\phi}_{sewi} - \frac{V^2}{R_{wi}}\phi_{sewi}] = F_{fzLi} + F_{fzRi} - F_{ezLi} - F_{ezRi} + M_{w2}g \tag{17}$$

$$F_{ezL,Ri} = K_{ez}(Z_{1wL,Ri} - Z_{2wi}) + C_{ez}(\dot{Z}_{1wL,Ri} - \dot{Z}_{2wi}) \tag{18}$$

$$F_{eyL,Ri} = K_{ey}(Y_{1wL,Ri} - Y_{2wi}) + C_{ey}(\dot{Y}_{1wL,Ri} - \dot{Y}_{2wi}) \tag{19}$$

where M_{w1} and M_{w2} are the mass of the rim and the rest parts of the wheelset as shown in Figure 5. $\ddot{Y}_{1wL,Ri}$, \ddot{Y}_{2wi} , $\ddot{Z}_{1wL,Ri}$, and \ddot{Z}_{2wi} are accelerations of rim and the rest parts of the wheelset. Y indicates lateral response, and Z indicates vertical response. $\dot{Y}_{1wL,Ri}$, \dot{Y}_{2wi} , $\dot{Z}_{1wL,Ri}$ and \dot{Z}_{2wi} are velocities of rim and the rest parts of the wheelset. $Y_{1wL,Ri}$, Y_{2wi} , $Z_{1wL,Ri}$ and Z_{2wi} are displacements of rim and the rest parts of the wheelset. V is the running speed. R_{wi} is the curve radii of i -th wheel. a_0 is the half of the distance between left and right nominal rolling circles. $\ddot{\phi}_{sewi}$ and ϕ_{sewi} are the angular acceleration and angular of super-elevation. $F_{eyL,Ri}$, $F_{wryL,Ri}$, and $F_{fyL,Ri}$ are lateral forces due to the stiffness and damping of rubber, due to wheel/rail interaction, and due to primary suspension system. $F_{ezL,Ri}$,

$F_{wzL,Ri}$, and $F_{fzL,Ri}$ are vertical forces due to the stiffness and damping of rubber, due to wheel/rail interaction, and due to primary suspension system.

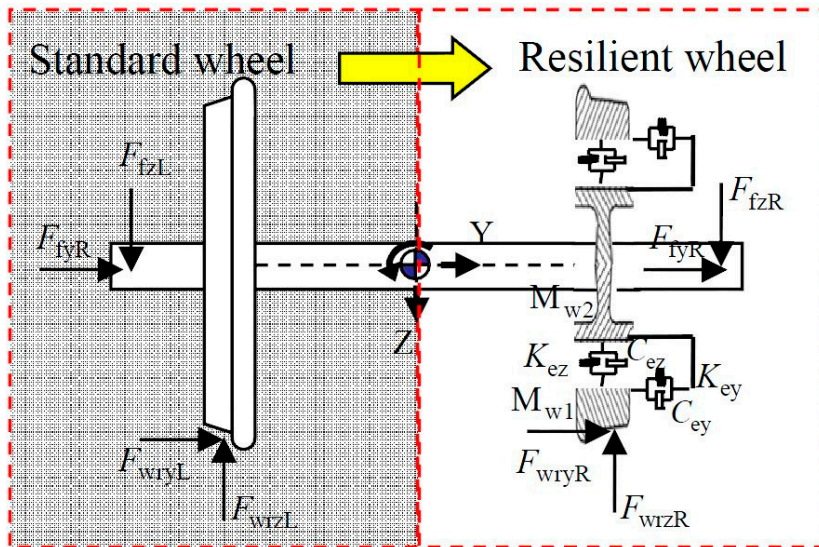


Figure 5. Dynamic model of resilient wheel.

2.2. The Transient Finite and Boundary Element Model for Wheel/Rail Vibration and Sound Radiation

Three-dimensional (3D) finite element (FE) models of a standard metro wheel and a conventional slab track were developed to obtain the vibrations (Figure 6). In the model, the normal forces and lateral creep forces obtained by the vehicle/track interaction dynamic model in Section 2.1 are applied to the tread of wheelset and rail head. Figure 6 also shows the FE models of resilient wheel and embedded track to analyze their effect on wheel/rail noise attenuation under lateral excitation. The FE model was developed in commercial software ANSYS.

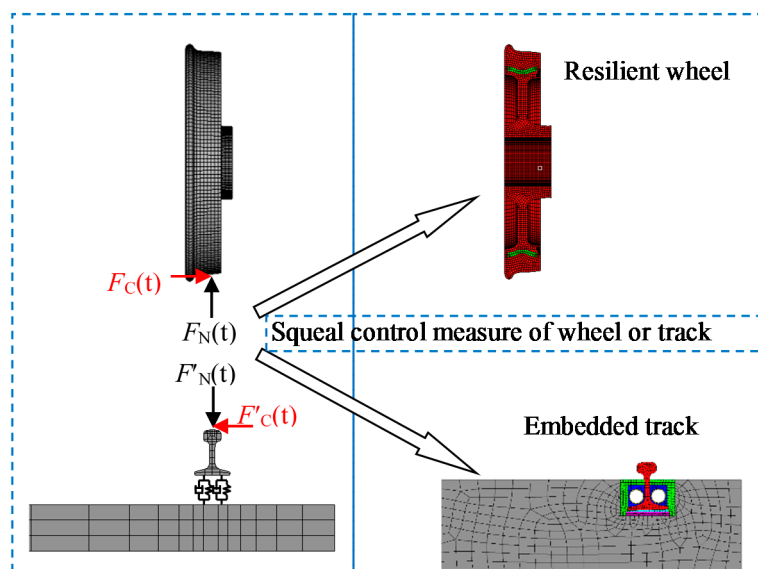


Figure 6. Dynamic model of resilient wheel and embedded rail.

Once the vibrations of the wheel and track are determined using by 3D FE model, sound radiations from the wheel and track can be evaluated using an appropriate vibro-acoustic prediction method.

There are three radiators: the wheels, the rails and the slabs. Equation (20) shows the 3D acoustic integral equation [36] for a sound field of frequency ω .

$$\bar{p}(x, y, z) = - \int_S \left(\bar{p}(x', y', z') \frac{\partial G(R)}{\partial n} + i\rho\omega G(R)v_n(x', y', z') \right) dS \tag{20}$$

where $\bar{p}(x, y, z)$ denotes sound pressure amplitude in the acoustic domain, $v_n(x', y', z')$ denotes air particle velocity amplitude in the normal direction of the domain boundary (the unit normal vector of the boundary, denoted by n , is pointing out of the domain, and finally,

$$G(R) = \frac{e^{-ikR}}{4\pi R}, R = \sqrt{(x - x')^2 + (y - y')^2 + (z - z')^2} \tag{21}$$

is the Green's function with the source at (x, y, z) and observer at (x', y', z') , and k is the wavenumber.

Equation (20) is solved by 3D boundary element method (BEM). Discrete boundary surface into several sub boundary elements Ω_{ae} . In this way, the distribution of sound pressure p and normal velocity v_n on the boundary surface is approximated to the sound pressure \hat{p} and normal velocity \hat{v}_n in a series of sub boundary elements. Then, the sound pressure p and normal velocity v_n can be written as:

$$p(x', y', z') \approx \hat{p}(x', y', z') = \sum_{i=1}^{n_e} N_i^e(x', y', z') \cdot a_{pi}, \quad (x', y', z') \in \Omega_{ae} \tag{22}$$

$$v_n(x', y', z') \approx \hat{v}_n(x', y', z') = \sum_{i=1}^{n_e} N_i^e(x', y', z') \cdot a_{vi}, \quad (x', y', z') \in \Omega_{ae} \tag{23}$$

The N_i^e is the shape function of node i . Defined that N_i^e is one at the node i , and zero at other nodes. a_{pi} and a_{vi} are the sound pressure and normal velocity of the node i .

Defined that $[N]$ is the $(1 \times n_a)$ matrix of shape function N_i^e . $\{\hat{p}_i\}$ is the $(n_a \times 1)$ matrix of sound pressure a_{pi} . $\{\hat{v}_{ni}\}$ is the $(n_a \times 1)$ matrix of normal velocity a_{vi} . Here n_a is the total number of nodes. $\hat{p}(x', y', z')$ and $\hat{v}_n(x', y', z')$ can be further written as:

$$\hat{p}(x', y', z') = [N] \cdot \{\hat{p}_i\}, \quad (x', y', z') \in \Omega_a \tag{24}$$

$$\hat{v}_n(x', y', z') = [N] \cdot \{\hat{v}_{ni}\}, \quad (x', y', z') \in \Omega_a \tag{25}$$

To use (24) and (25) solving Equation (20), the relationship of \hat{p}_i and \hat{v}_{ni} needs to be determined. The relationship of them can be written as:

$$[A_b]\{\hat{p}_i\} = j\rho_0\omega[B_b]\{\hat{v}_{ni}\} \tag{26}$$

The i th column element A_{bi} in the coefficient matrix $[A_b]$ can be expressed as:

$$A_{bi} = \delta_{bi} \cdot \left[1 + \frac{1}{4\pi} \int_{\Omega_a} \frac{\partial}{\partial n} \left(\frac{1}{|R_b|} \right) d\Omega_a \right] - \left[\int_{\Omega_a} N_i(x', y', z') \left(\frac{\partial G(R_b)}{\partial n} \right) d\Omega_a \right] \tag{27}$$

The i th column element B_{bi} in the coefficient matrix $[B_b]$ can be expressed as:

$$B_{bi} = \int_{\Omega_a} N_i(x', y', z') G(R_b) d\Omega_a \tag{28}$$

where $R_b = \sqrt{(x_b - x')^2 + (y_b - y')^2 + (z_b - z')^2}$. δ_{bi} is Kronecker symbol. If $b = i$, $\delta_{bi} = 1$, If $b \neq i$, $\delta_{bi} = 0$.

Considering boundary conditions, Equation (26) can be solved. Now the sound pressure of any point (x, y, z) in sound field can be determined by the sound pressure and normal velocity on the boundary surface.

$$p(x, y, z) = [C]\{\hat{p}_i\} + [D]\{\hat{v}_{ni}\} \tag{29}$$

The i th column element C_i in the coefficient matrix $[C]$ can be expressed as:

$$C_i = \int_{\Omega_a} N_i(x', y', z') \left(\frac{\partial G(R)}{\partial n} \right) d\Omega_a \tag{30}$$

The i th column element D_i in the coefficient matrix $[D]$. can be expressed as:

$$D_i = j\rho_o\omega \int_{\Omega_a} N_i(x', y', z') G(R) d\Omega_a \tag{31}$$

For the BE model of wheel, the hole left in the wheel hub is closed to model the effect of axle. For the BE model of track, sound radiation only considers rail and slab surface. For a railway on the ground surface, the acoustic domain may be approximated to be a half-space. It has two acoustically hard boundaries (the sound absorption effect of the ground surface will not be considered in this paper). They are the horizontal plane beyond the top surface of the slabs. Other boundaries of the acoustic domain are radiating, including the top surface of the slabs and the surfaces of the rails. Connections between the rails and the slabs are ignored, leaving a uniform gap between the rails and the slabs. The effect of the presence of a train on the sound field will not be considered in the current paper. Thus, the acoustic domain is uniform in the track direction.

3. Results and Discussions

3.1. Wheel/Rail Noise Prediction and Preliminary Validation

This section gives the wheel/rail force, acceleration and sound pressure level of the wheels under the wheel/rail force excitation with and without squealing phenomenon in a sharp curve. When a vehicle curves, the leading wheel (front wheel) has a potential to produce squeal and the trailing wheel (rear wheel) should not produce squeal.

Figure 7 gives the lateral creep force of the leading wheelset when a vehicle runs from a tangent line to a narrow circular curve at the speed of 45 km/h. The curve radius is 250 m, and the track cant is 96 mm. The main physical parameters of the metro vehicle used in the simulations are given in Table 1.

Table 1. Main parameters of metro vehicle.

Notations	Parameters	Values (End)
M/I	Body inertia	
M_c	Car body mass (kg)	2.16×10^4
M_b	Bogie mass (kg)	4.00×10^3
M_w	Wheelset mass (kg)	1.86×10^3
I_{cx}	Car body roll moment of inertia (kg·m ²)	3.11×10^4
I_{cy}	Car body pitch moment of inertia (kg·m ²)	8.61×10^5
I_{cz}	Car body yaw moment of inertia (kg·m ²)	8.56×10^5
I_{bx}	Bogie roll moment of inertia (kg·m ²)	1.19×10^3
I_{by}	Bogie pitch moment of inertia (kg·m ²)	8.76×10^2
I_{bz}	Bogie yaw moment of inertia (kg·m ²)	2.10×10^3
I_{wx}	Wheelset roll moment of inertia (kg·m ²)	1.04×10^3
I_{wy}	Wheelset pitch moment of inertia (kg·m ²)	1.37×10^2
I_{wz}	Wheelset yaw moment of inertia (kg·m ²)	1.04×10^3

Table 1. Cont.

Notations	Parameters	Values (End)
K/C	Primary suspension	
K_{px}	Longitudinal stiffness (MN/m)	17.62
K_{py}	Lateral stiffness (MN/m)	9.62
K_{pz}	Vertical stiffness (MN/m)	0.60
C_{pz}	Vertical damping coefficient (kN·s/m)	13.00
K/C	Secondary suspension	
K_{sx}	Longitudinal stiffness (MN/m)	0.16
K_{sy}	Lateral stiffness (MN/m)	0.16
K_{sz}	Vertical stiffness (MN/m)	1.39
C_{sy}	Lateral damping coefficient (kN·s/m)	23.00
C_{sz}	Vertical damping coefficient (kN·s/m)	25.00
$L/D/H$	Dimension	
R_w	Wheel radius (m)	0.42
L_v	Vehicle length (m)	19.5
L_b	Distance between two axles of a bogie (m)	2.3
L_c	Distance between two bogie centers (m)	12.6
D_{ps}	Lateral span of primary suspensions (m)	2.01
D_{ss}	Lateral span of secondary suspensions (m)	1.9
H_{bw}	Height of bogie centre from wheelset centre (m)	0.069
H_{cb}	Height of car body centre from bogie centre (m)	1.37

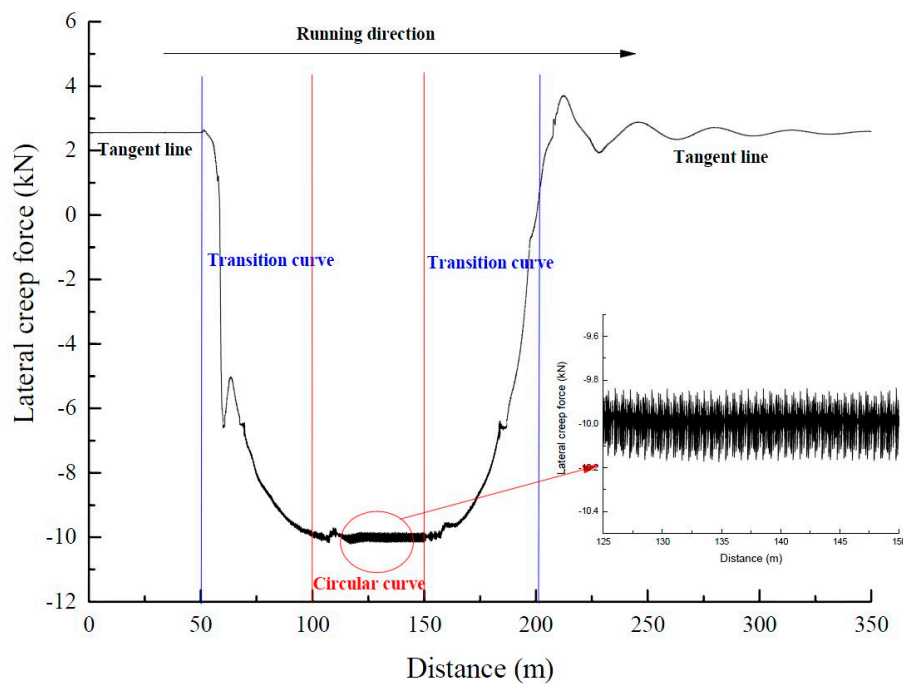


Figure 7. Lateral creep force of the leading wheelset when a vehicle negotiates a narrow curve (simulation results).

It can be seen from Figure 7 that the lateral creep force is very stable at tangent line. In addition, the fluctuation of lateral creep force increases gradually from transition curve to circular curve, and reaches maximum when the vehicle negotiates the circular curve. Figure 8 shows the lateral creep forces of leading and trailing wheels. It can be seen that the fluctuation of lateral creep force of leading wheel is larger than trailing wheel.

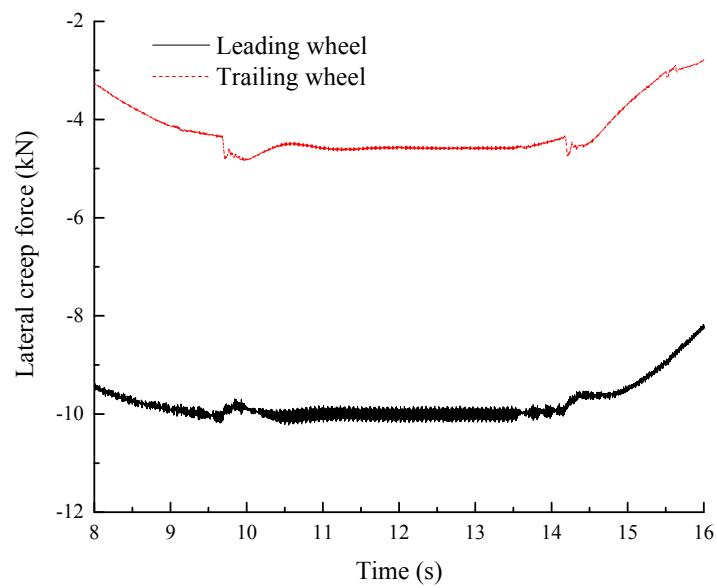


Figure 8. Lateral creep force of leading wheel and trailing wheel (simulation results).

Figure 9a,b give the acceleration of leading inner wheel and trailing inner wheel in time domain and frequency domain. It can be seen that the acceleration of the leading inner wheel with squeal is much larger than that of trailing inner wheel without squeal. In addition, highest peaks occur at modal frequencies corresponding to axial modes with zero-nodal-circle, showing that these modes are easy to be excited during curving. The axial mode shapes of wheel are expressed as (m, n) . m represents number of nodal circle. n represents number of nodal diameter. For example, $(0, 1)$ represents zero-nodal-circle with one-nodal-diameter. Thus, the frequencies and corresponding axle mode shapes are 265 Hz $(0, 1)$, 353 Hz $(0, 0)$, 468 Hz $(0, 2)$, 1167 Hz $(0, 3)$, and 2008 Hz $(0, 4)$. These frequencies by simulation in this paper have a good agreement with the FRF test in the semi-anechoic room [8].

Figure 10a,b give the sound pressure level (SPL) (at the point which is 30 cm away from the outside of wheel tyre) of leading wheel and trailing wheel in time domain and frequency domain. It can be seen that the SPL of the leading wheel with squeal is much higher than that of trailing wheel at frequencies of axial modes.

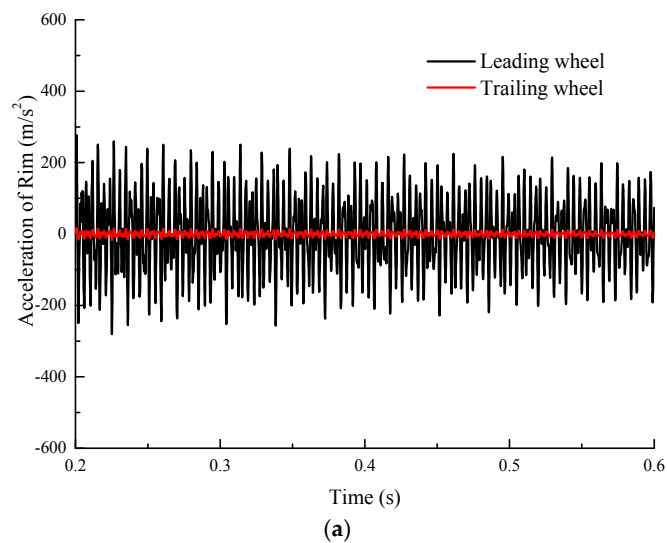


Figure 9. Cont.

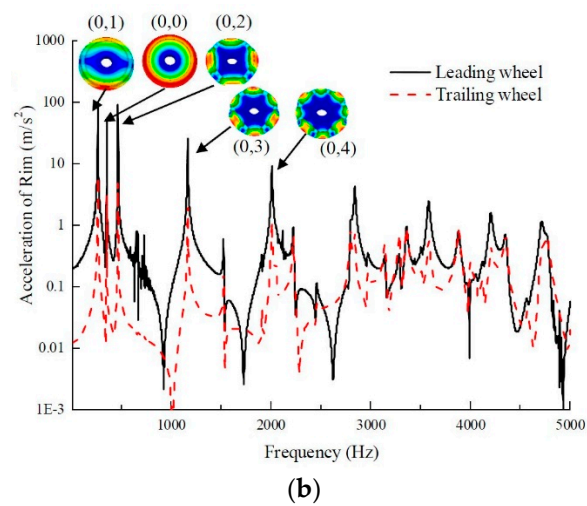


Figure 9. Acceleration of leading wheel and trailing wheel in (a) time domain and (b) frequency domain (simulation results).

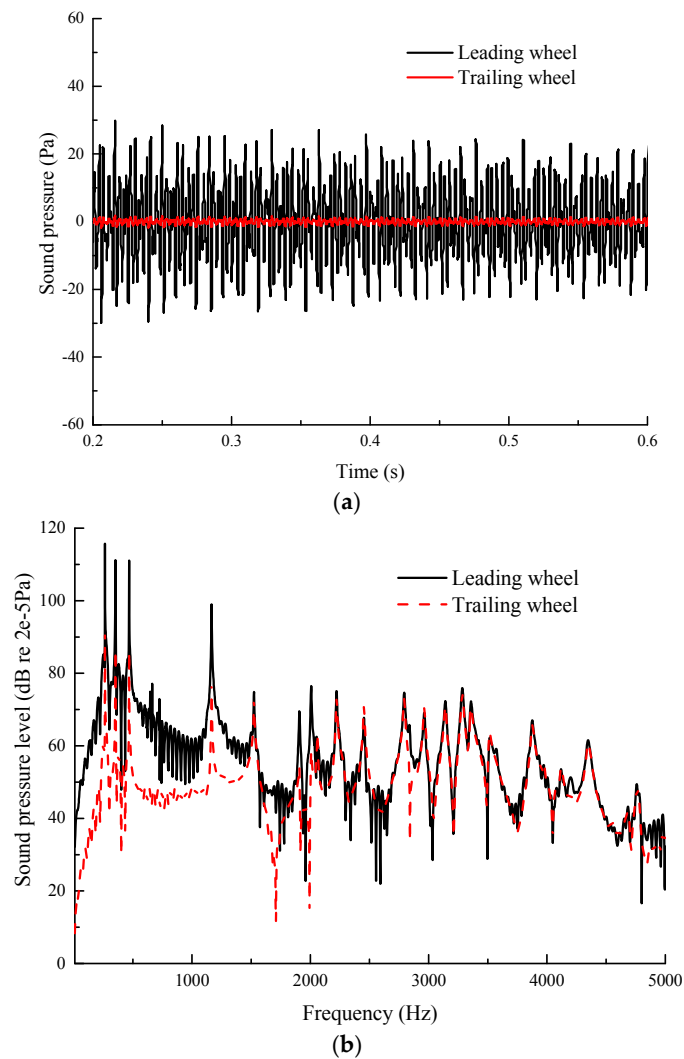


Figure 10. SPLs at a distance of 30 cm from the leading and trailing wheels in (a) time domain and (b) frequency domain (simulation results).

Wheel/rail noise is also tested near a wheel (860 mm diameter) used in metro when the vehicle passes a sharp curve (radius = 250 m) at the speed of 45 km/h. The microphone is arranged in the outside of the leading wheel with the distance of 30 cm, which is shown in Figure 11. In the process of field test, squealing noise can be heard clearly. Figure 12 gives comparison between simulation and experimental results of SPL of the leading wheel with the same curve radius and running speed.

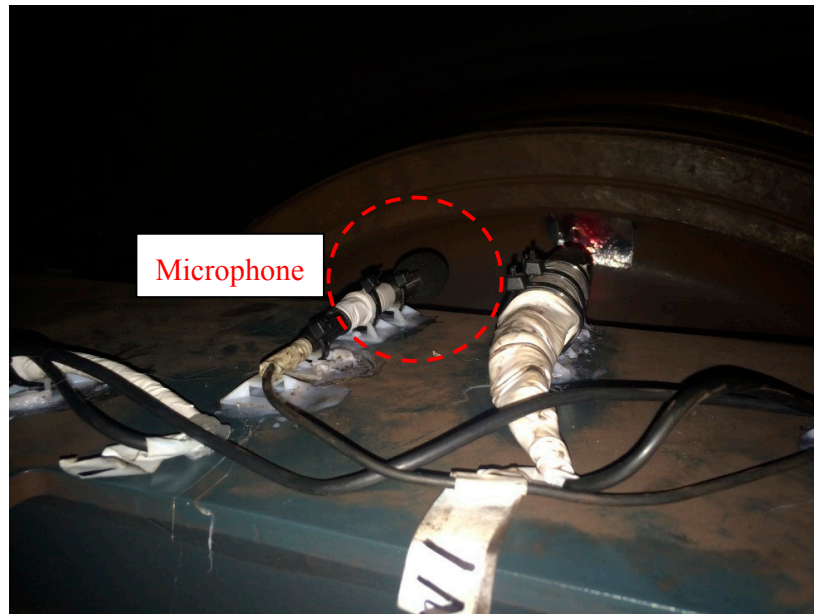


Figure 11. Microphone arrangement.

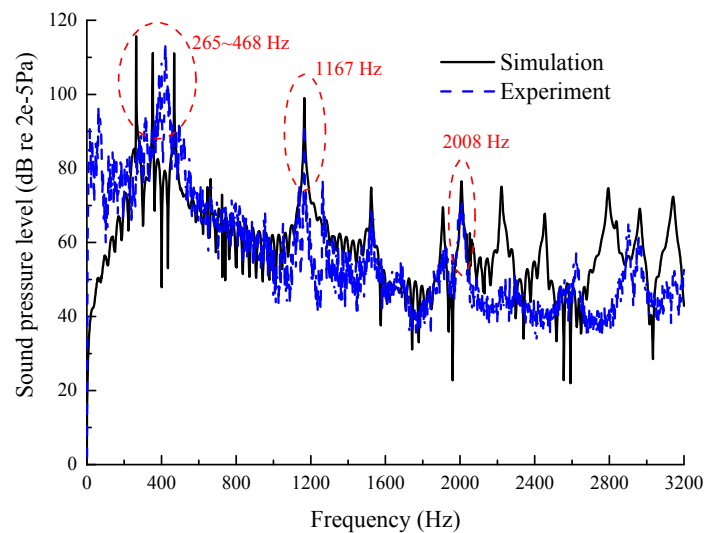


Figure 12. Comparison between simulation and experimental results of SPL of the leading wheel.

Figure 12 shows that the SPL at the frequencies of 265–468, 1167, 2008 Hz are significant for both simulation and experimental results. These frequencies have a good agreement with the zero-nodal-circle and n-nodal-diameter axial wheel modes for simulation and experimental results. Amplitude difference percentages between simulation and experiment of 265–468, 1167, and 2008 Hz are 3%, 7%, and 6.5% of their corresponding peaks, respectively. The differences mainly come from the simplification and assumption of the actual situation from the simulation model. In other words, the current model can predict all squeal frequencies and give relatively accurate amplitudes of them.

Thus, this simplified model can be used for regular investigation on wheel/rail noise when the vehicle curves.

3.2. Effect of Wheel/Rail Friction Coefficients on Wheel/Rail Noise under Lateral Excitation

This section investigates the effect of friction coefficient between wheel and rail on vibration and wheel/rail noise under lateral excitation. The friction coefficient of 0.012–0.3 are chosen for analysis because they cover the range of common friction coefficients. The value of 0.3 represents dry friction coefficient. The value of 0.012 represents the friction coefficient considering the third medium—oil between wheel/rail interface. The values of 0.1 and 0.05 represent friction coefficients between dry status and oil status.

Figure 13a,b give the lateral accelerations of leading wheel with different friction coefficients in time domain and frequency domain. It can be seen that the acceleration decreases obviously at curve squeal frequencies as the friction coefficient increase. Figure 14a,b give the SPLs with different friction coefficients in time domain and frequency domain. It can be seen that SPLs also have a good reduction in significant peaks after reducing the friction coefficient. The sound reduction (SPL) of wheel considering lubricant can reduce 10–25 dB corresponding to the friction coefficient of 0.012–0.05, compared with the SPL of friction coefficient of 0.3. Therefore, it suggests that proper lubrication between the wheel and rail interface can reduce squeal noise effectively.

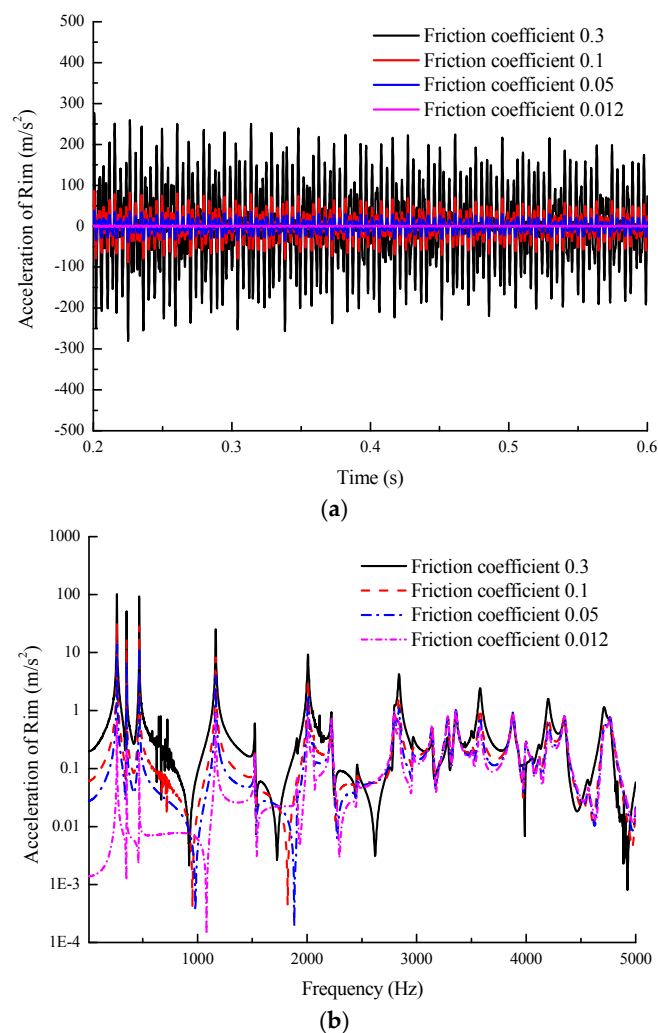


Figure 13. Accelerations with different friction coefficients in (a) time domain and (b) frequency domain (simulation results).

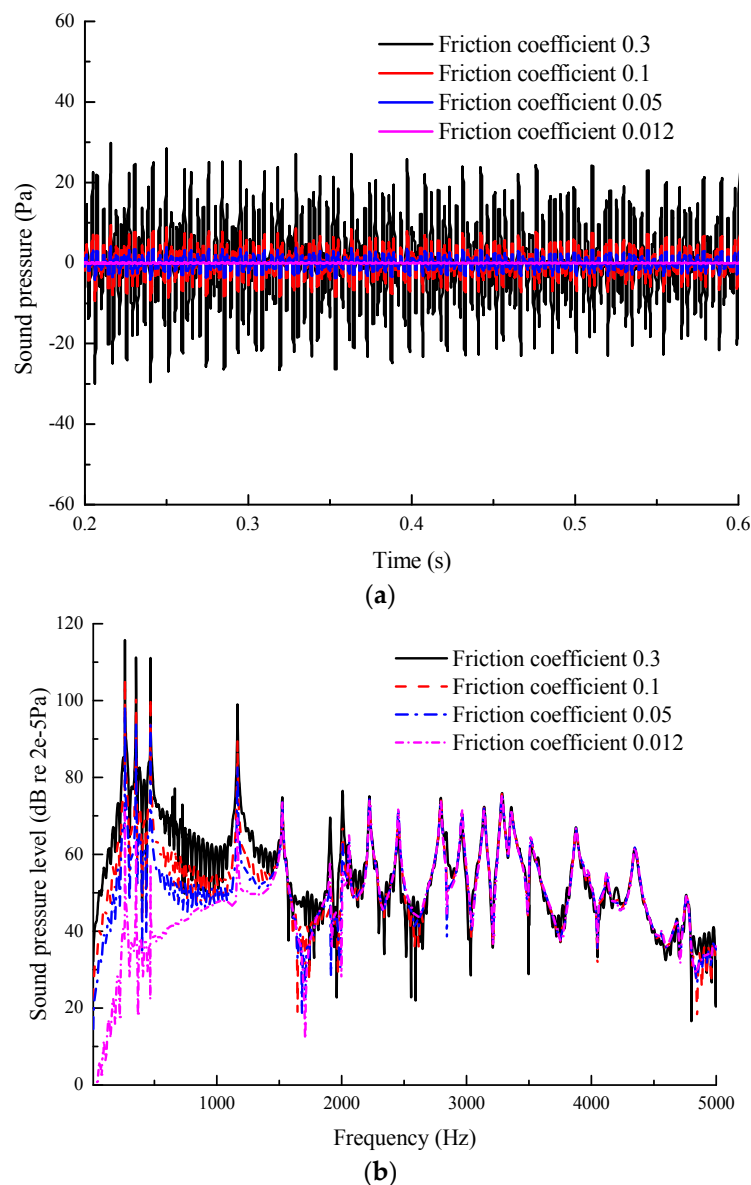


Figure 14. SPLs with different friction coefficients in (a) time domain and (b) frequency domain (simulation results).

3.3. Effect of Embedded Track on Wheel/Rail Noise under Lateral Excitation

This section investigates the effect of embedded track on wheel/rail noise under lateral excitation. The SPL of embedded track is calculated based on the embedded track dynamic model and transit BEM model in Sections 2.1 and 2.2. Figure 15 shows the SPLs of track comparison between conventional slab track and embedded track. It can be seen that the SPL of embedded track without considering wheel has a very good reduction in broad bands due to its damping of the elastic material around the rail absorbs vibration and then resulting in a low noise.

Figure 16 gives the total SPLs considering standard metro wheels coupled with the conventional slab track and embedded track respectively. It can be seen that when the embedded track coupled with a squealing wheel, the reduction of sound is limited (about 2–3 dB) because the wheel is the main sound radiation source when squeal occurs, as is shown in Figure 17. In Figure 7, the SPL of a standard metro wheel is compared with the embedded track because the contribution of wheel/rail noise must be clear. The SPL of the standard metro wheel is larger than that of track in a wide frequency domain

which contributes significantly to the total value of wheel-rail noise. Although the embedded track is not significant on the reduction of wheel/rail noise in the curve, it may have more effect on reducing rolling noise [37,38].

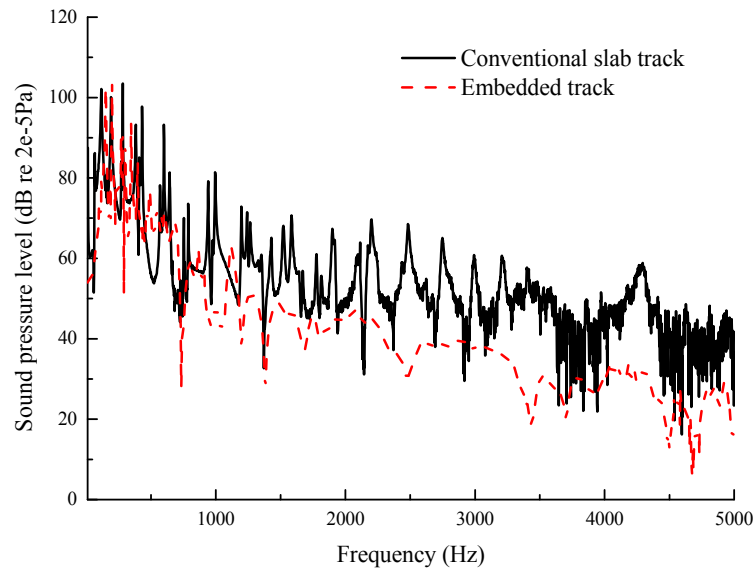


Figure 15. SPLs of track comparison between conventional slab track and embedded track (simulation results).

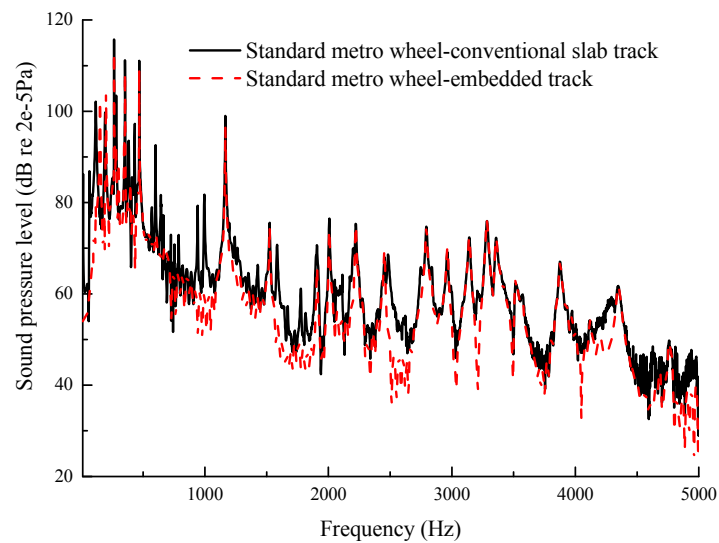


Figure 16. Total SPLs considering standard metro wheels coupled with the conventional slab track and embedded track (simulation results).

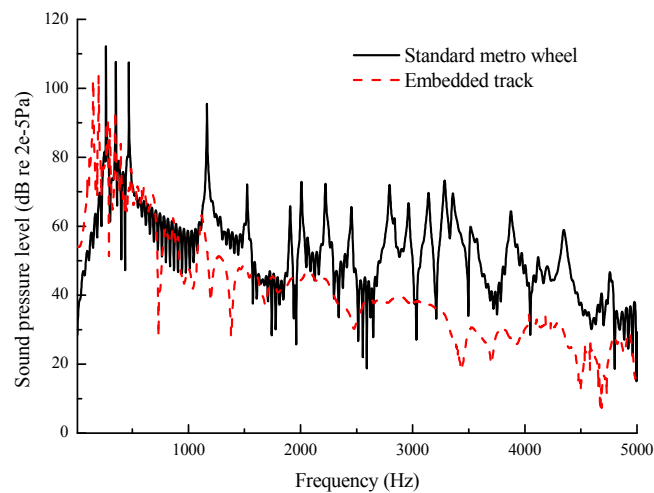


Figure 17. SPL compare between standard metro wheel and embedded track (simulation results).

3.4. Effect of Resilient Wheel on Wheel/Rail Noise under Lateral Excitation

This section investigates the effect of resilient wheel on wheel/rail noise under lateral excitation. The SPL of resilient wheel is calculated based on the resilient wheel dynamic model and transit BEM model in Sections 2.1 and 2.2. Figure 18 shows the SPLs of wheel comparison between the standard wheel and the resilient wheel. It can be seen that the resilient wheel has a very good reduction in sharp peaks, especially for the peaks of squeal frequencies, due to high damping in the resilient wheel and decoupling of the rim and web.

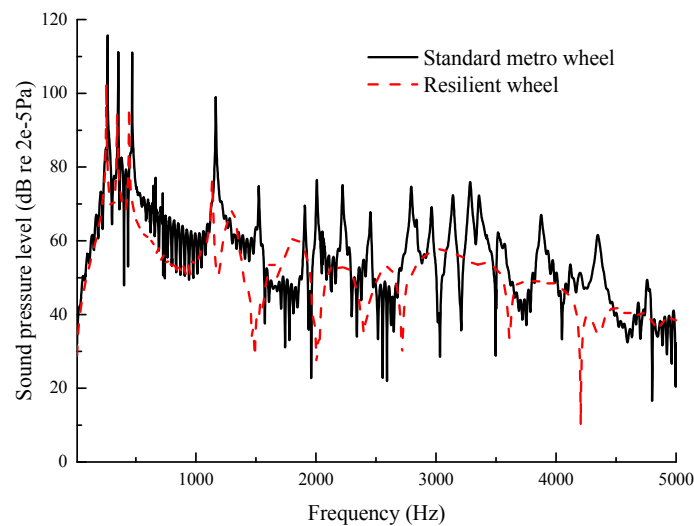


Figure 18. SPL compare between standard metro wheel and elastic wheel (simulation results).

Figure 19 gives the total SPLs of conventional slab track coupled with the standard metro wheel and resilient wheel respectively. It can be seen that when the resilient wheel coupled with the conventional slab track, the reduction of sound is significant (about 5–6 dB) because the resilient wheel can reduce squeal noise of wheel, which is main source for squeal noise, namely the main sound source is controlled. Thus, the total SPLs is reduced by using resilient wheel.

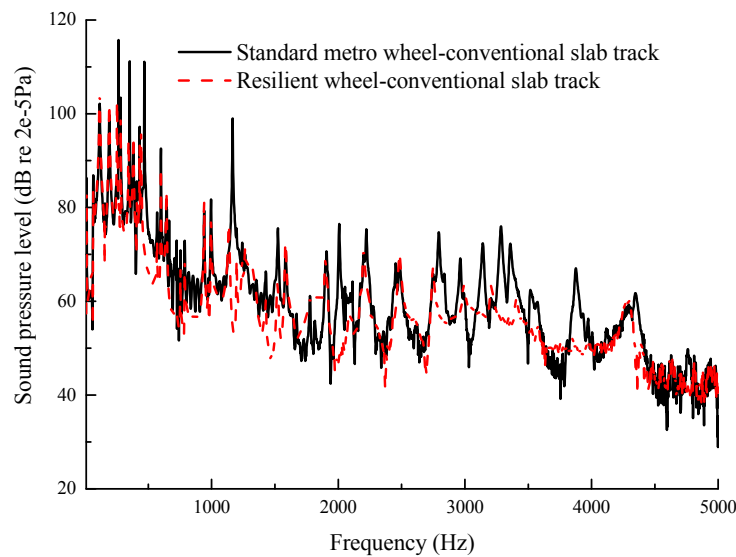


Figure 19. SPLs of common slab track coupled with the standard metro wheel and elastic wheel (simulation results).

4. Conclusions

A vehicle-track coupling dynamic model considering the falling wheel/rail friction coefficients was built to study the wheel/rail contact in narrow curve. In addition, a transient finite element and boundary element time domain models of vibration and sound were developed for sound radiation evaluation. Wheel/track vibration and sound pressure response are presented for a vehicle negotiating a narrow curve. The following conclusions can be drawn:

- (1) Different wheels have different levels of wheel/rail noise when the vehicle curves. The wheel/rail noise of the leading wheel is 20 dB larger than that of the trailing wheel.
- (2) Proper lubrication in wheel/rail interface can effectively reduce wheel/rail noise when the vehicle curves. The sound reduction of wheel considering lubricant (friction coefficient: 0.012~0.1) can reduce 10~25 dB compared to that of friction coefficient 0.3.
- (3) The application of vibration and noise control measures on wheels is better than that on track when the vehicle curves. The total sound reduction of the embedded track coupled with a squealing wheel is about only 2–3 dB. However, the total sound reduction of the elastic wheel coupled with the conventional slab track is about 5–6 dB.

Acknowledgments: This study was supported by the National Key R & D Program of China (2016YFB1200503-02, 2015BAG13B01-03) and the National Natural Science Foundation of China (U1134202, 51305360, 51475390).

Author Contributions: Guotang Zhao and Xuesong Jin conceived and designed the simulations and experiments; Jian Han, Yuanpeng He, and Xinbiao Xiao performed the numerical simulations and experiments; Jian Han and Xiaozhen Sheng analyzed the data; Jian Han wrote the paper.

Conflicts of Interest: The authors declare no conflict of interest.

References

1. Rudd, M. Wheel/rail noise—Part 2: Wheel squeal. *J. Sound Vib.* **1976**, *46*, 381–394. [[CrossRef](#)]
2. Thompson, D.J.; Jones, C.J.C. A review of the modelling of wheel-rail noise generation. *J. Sound Vib.* **2000**, *231*, 519–536. [[CrossRef](#)]
3. Brunel, J.F.; Dufrénoy, P.; Naït, M.; Muñoz, J.L.; Demilly, F. Transient models for curve squeal noise. *J. Sound Vib.* **2006**, *293*, 758–765. [[CrossRef](#)]

4. Kooijman, P.P.; Van Vliet, W.J.; Janssens, M.H.A.; de Beer, F.G. Curve squeal of railbound vehicles—Part 2: Set-up for measurement of creepage dependent friction coefficient. In Proceedings of the Internoise 2000, Nice, France, 27–30 August 2000.
5. Eadie, D.T.; Santoro, M. Top-of-rail friction control for curve noise mitigation and corrugation rate reduction. *J. Sound Vib.* **2006**, *293*, 747–757. [[CrossRef](#)]
6. Wetta, P.; Demilly, F. Reduction of wheel squeal noise generated on curves or during braking. In Proceedings of the 11th International Wheelset Congress, Paris, France, 18–22 June 1995.
7. Brunel, J.F.; Dufrenoy, P.; Demilly, F. Modelling of squeal noise attenuation of ring damped wheels. *J. Sound Vib.* **2004**, *65*, 457–471. [[CrossRef](#)]
8. Han, J.; Wen, Z.; Wang, R.; Wang, D.; Xiao, X.; Zhao, G.; Jin, X. Experimental study on vibration and sound radiation reduction of the web-mounted noise shielding and vibration damping wheel. *Noise Control Eng. J.* **2014**, *62*, 110–122. [[CrossRef](#)]
9. Liu, H.; Yang, J.; Wu, T. The influences of rail vibration absorber on normal wheel-rail contact forces due to multiple wheels. *J. Vib. Control* **2015**, *21*, 275–284. [[CrossRef](#)]
10. Ruiten, C.J.M. Mechanism of squeal noise generated by trams. *J. Sound Vib.* **1988**, *120*, 245–253. [[CrossRef](#)]
11. Remington, P.J. Wheel/rail squeal and impact noise: What do we know? What do not we know? Where do we go from here? *J. Sound Vib.* **1985**, *116*, 339–353. [[CrossRef](#)]
12. Schneider, E.; Popp, K.; Irretier, H. Noise generation in railway wheels due to rail-wheel contact forces. *J. Sound Vib.* **1988**, *120*, 227–244. [[CrossRef](#)]
13. Fingberg, U. A model of wheel-rail squealing noise. *J. Sound Vib.* **1990**, *143*, 365–377. [[CrossRef](#)]
14. Périard, F. Wheel-Rail Noise Generation: Curve Squealing by Trams. Ph.D. Thesis, Technische Universiteit, Delft, The Netherlands, 1998.
15. Heckl, M.A.; Abrahams, I.D. Curve squeal of train wheels, part 1: Mathematical model for its generation. *J. Sound Vib.* **2000**, *229*, 669–693. [[CrossRef](#)]
16. Beer, F.G.; Janssens, M.H.A.; Kooijman, P.P. Squeal noise of rail-bound vehicles influenced by lateral contact position. *J. Sound Vib.* **2003**, *267*, 497–507. [[CrossRef](#)]
17. Monk-Steel, A.D.; Thompson, D.J. Models for railway curve squeal noise. In Proceedings of the 8th Conference on Recent Advances in Structural Dynamics, Southampton, UK, 14–16 July 2003.
18. Chiello, O.; Ayasse, J.B.; Vincent, N.; Koch, J.R. Curve squeal of urban rolling stock- Part 3: Theoretical model. *J. Sound Vib.* **2006**, *293*, 710–727. [[CrossRef](#)]
19. Cataldi-Spinola, E.; Glocker, C. Curve squealing of railroad vehicles. In Proceedings of the ENOC-2005, Eindhoven, The Netherlands, 7–12 August 2005.
20. Kalker, J.J. Survey of wheel-rail rolling contact theory. *Veh. Syst. Dyn.* **1979**, *5*, 317–358. [[CrossRef](#)]
21. Xie, G.; Allen, P.D.; Iwnicki, S.D.; Alonso, A.; Thompson, D.J.; Jones, C.J.; Huang, Z.Y. Introduction of falling friction coefficients into curving calculations for studying curve squeal noise. *Veh. Syst. Dyn.* **2006**, *44* (Suppl. 1), S261–S271. [[CrossRef](#)]
22. Thompson, D.J.; Janssens, M.H.A. *Theoretical Manual, Version 2.4*; TNO Report, No. TPD-HAG-RPT-930214 (Revised); TNO: Hague, The Netherlands, 1997.
23. Huang, Z. Theoretical Modelling of Railway Curve Squeal. Ph.D. Thesis, University of Southampton, Southampton, UK, 2007.
24. Hoffmann, N.; Fischer, M.; Allgaier, R.; Gaul, L. A minimal model for studying properties of the mode-coupling type instability in friction induced oscillations. *Mech. Res. Commun.* **2002**, *29*, 197–205. [[CrossRef](#)]
25. Hoffmann, N.; Gaul, L. Effects of damping on mode-coupling instability in friction induced oscillations. *J. Appl. Math. Mech.* **2003**, *83*, 524–534. [[CrossRef](#)]
26. Sinou, J.J.; Jezequel, L. Mode coupling instability in friction-induced vibrations and its dependency on system parameters including damping. *Eur. J. Mech.-A/Solids* **2007**, *26*, 106–122. [[CrossRef](#)]
27. Thompson, D.J.; Squicciarini, G.; Ding, B. A state-of-the-art review of curve squeal noise: Phenomena, mechanisms, modelling and mitigation. In Proceedings of the 12th International Workshop on Railway Noise, Terrigal, Australia, 12–16 September 2016.
28. Jin, X.S.; Wen, Z.F. Effect of discrete track support by sleepers on rail corrugation at a curved track. *J. Sound Vib.* **2007**, *315*, 279–300. [[CrossRef](#)]

29. Xiao, X.B.; Jin, X.S.; Wen, Z.F. Effect of disabled fastening systems and ballast on vehicle derailment. *J. Vib. Acoust.* **2007**, *129*, 217–229. [[CrossRef](#)]
30. Han, J.; Zhao, G.T.; Xiao, X.B.; Wen, Z.F.; Guan, Q.H.; Jin, X.S. Effect of softening of cement asphalt mortar on vehicle operation safety and track dynamics. *J. Zhejiang Univ. SCIENCE A* **2015**, *16*, 976–986. [[CrossRef](#)]
31. Han, J.; Zhao, G.T.; Sheng, X.Z.; Jin, X.S. Study on the subgrade deformation under high-speed train loading and water-soil interaction. *Acta Mech. Sin.* **2016**, *32*, 233–243. [[CrossRef](#)]
32. Ling, L.; Dhanasekar, M.; Thambiratnam, D.P.; Sun, Y.Q. Lateral impact derailment mechanisms, simulation and analysis. *Int. J. Impact Eng.* **2016**, *94*, 36–49. [[CrossRef](#)]
33. Ling, L.; Dhanasekar, M.; Thambiratnam, D.P.; Sun, Y.Q. Minimising lateral impact derailment potential at level crossings through guard rails. *Int. J. Mech. Sci.* **2016**, *113*, 49–60. [[CrossRef](#)]
34. Zhai, W.M. Two simple fast integration methods for large-scale dynamic problems in engineering. *Int. J. Numer. Methods Eng.* **1996**, *39*, 4199–4214. [[CrossRef](#)]
35. Shen, Z.Y.; Hedrick, J.K.; Elkins, J.A. A comparison of alternative creep-force models for rail vehicle dynamic analysis. *Veh. Syst. Dyn.* **1983**, *12*, 79–83. [[CrossRef](#)]
36. Wu, T.W. *Boundary Element Acoustics*; WIT Press: Southampton, UK, 2005.
37. Ling, L.; Han, J.; Xiao, X.; Jin, X. Dynamic behavior of an embedded rail track coupled with a tram vehicle. *J. Vib. Control* **2017**, *23*, 2355–2372. [[CrossRef](#)]
38. Zhao, Y.; Li, X.; Lv, Q.; Jiao, H.; Xiao, X.; Jin, X. Measuring, modelling and optimising an embedded rail track. *Appl. Acoust.* **2017**, *116*, 70–81. [[CrossRef](#)]



© 2017 by the authors. Licensee MDPI, Basel, Switzerland. This article is an open access article distributed under the terms and conditions of the Creative Commons Attribution (CC BY) license (<http://creativecommons.org/licenses/by/4.0/>).